OPEN

Correspondence and requests for materials should be addressed to X.M.L. (liuxm@opt.ac.cn)

# Electrically tunable graphene plasmonic quasicrystal metasurfaces for transformation optics

Chao Zeng, Xueming Liu & Guoxi Wang

State Key Laboratory of Transient Optics and Photonics, Xi'an Institute of Optics and Precision Mechanics, Chinese Academy of Sciences, Xi'an 710119, China.

The past few years have witnessed tremendous achievements of transformation optics applied to metallic plasmonic systems. Due to the poor tunability of metals, however, the ultimate control over surface plasmons remains a challenge. Here we propose a new type of graphene plasmonic (GP) metasurfaces by shaping the dielectrics underneath monolayer graphene into specific photonic crystals. The radial and axial gradient-index (GRIN) lenses are implemented to demonstrate the feasibility and versatility of the proposal. It is found that the designed GP-GRIN lenses work perfectly well for focusing, collimating, and guiding the GP waves. Especially, they exhibit excellent performances in the THz regime as diverse as ultra-small focusing spot ($\lambda_0/60$) and broadband electrical tunability. The proposed method offers potential opportunities in exploiting active transformational plasmonic elements operating at THz frequencies.

Transformation optics has been proved to be a general methodology for taming and controlling electromagnetic waves in any desired manner[1]. Due to the capabilities to break through the Abbe's diffraction limit and implement tight field confinement, surface plasmon polaritons (SPPs) have triggered a large number of applications at subwavelength scale[2–4]. Transformation plasmonics renders a viable path toward the realization of on-chip transformation nanophotonic devices[5–8]. Over the past few years, plasmonic gradient-index (GRIN) lenses, with the advantages of being flat and free of geometrical aberrations, have been extensively investigated theoretically and experimentally[7–10]. For instance, Liu *et al.* theoretically proposed an efficient method to mold SPPs bound at metal/dielectric interfaces[7]. They demonstrated that by precisely tailoring the topology of a dielectric layer on top of a metal, the propagation of SPPs can be flexibly manipulated. Valle and Longhi reported a parabolic GRIN waveguide for subwavelength self-imaging and focusing of the SPP waves, and a cross-connect device and an efficient waveguide launcher were numerically demonstrated[9]. Zentgraf *et al.* experimentally validated the feasibility of the plasmonic Luneburg lens and Eaton lens for focusing and bending SPPs by modifying the dielectric material adjacent to the metal surface[10]. To date, the majorities of the transformational plasmonic devices are on the basis of metal/dielectric model, their limited tunability and increased losses at lower frequencies, inevitably, make metallic plasmonics less appealing for applications in the THz and mid-infrared regime[11,12].

Since the discovery of easy fabrication processes for remarkably high-quality monolayer graphene by Novoselov *et al.* in 2004, enormous efforts have been rapidly devoted to the emerging field of graphene[13–15]. With striking electrical and optical properties, a variety of graphene-based devices have been explored, such as modulators[16–18], photodetectors[19–21], and cloak[22]. Recently, graphene has been shown to support transverse-magnetic (TM) SPP modes at subwavelength scale for frequencies ranging from THz to the visible[23–26]. As a novel plasmonic material, graphene possesses unprecedented advantages over metals, including flexible tunability, extremely tight confinement, and low losses at THz and mid-infrared frequencies. Meanwhile, an increasing number of researches have focused on the hotspot of graphene plasmonics (GPs)[27–32]. For example, Vakil and Engheta reported that by designing spatially inhomogeneous and nonuniform conductivity patterns, graphene could be regarded as a one-atom-thick platform for transformation optical devices[24,25]. Chen *et al.* experimentally investigated the propagation of GP waves in tapered graphene nanostructures using near-field scattering microscopy[28]. They demonstrated that the wavelength of GP waves was more than 40 times smaller than the wavelength of illumination, and the GP waves exhibited extremely small mode volume as well as electrical tunability. All of the aforementioned works have theoretically and experimentally proved that graphene can serve as an ideal flatland platform for two-dimensional (2D) plasmonic photonic circuits.
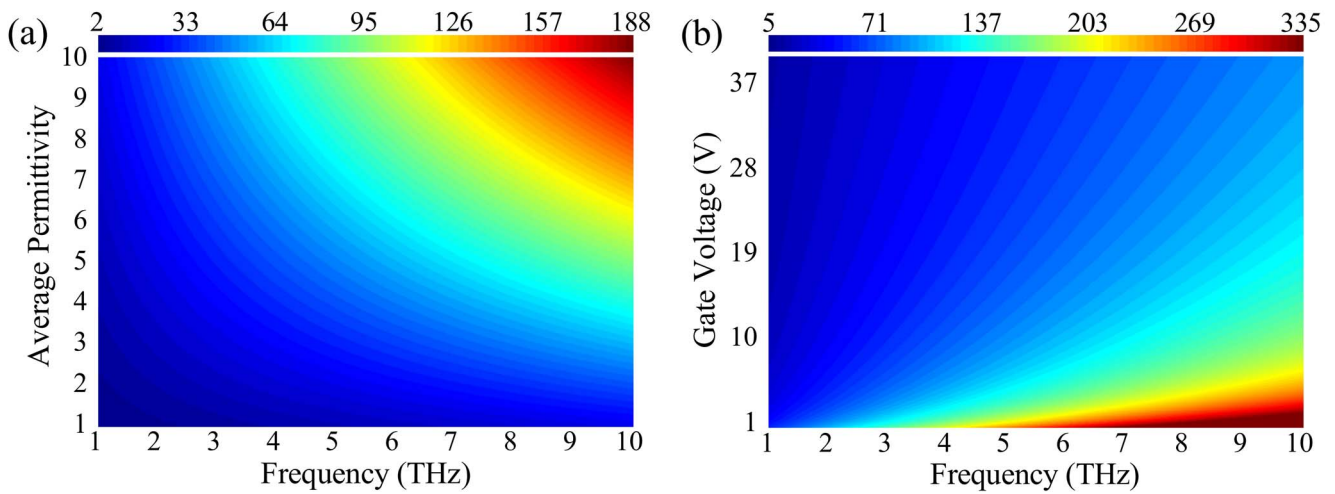
Figure 1 | Mode index evolution of the guided GP waves. (a) Dependence of GP mode index on the average permittivity of surrounded dielectrics for different frequencies with $E_f = 0.15$ eV (corresponds to the gate voltage of 20 V). (b) Dependence of GP mode index on the gate voltage for different frequencies with $\varepsilon_{avg} = 4$. The Fermi energy above the half of the maximum photon energy ($E_f > 0.02$ eV, corresponds to the gate voltage of 1 V) is taken into consideration in (b). The carrier mobility $\mu = 60000$ cm²V⁻¹s⁻¹ is utilized in the calculations.

In this paper, we propose a flexible design of graphene plasmonic quasicrystal (GPQ) metasurfaces by using the specific photonic-crystal (PC)-like dielectric layer underneath a graphene sheet. Based on the proposal, the GP-GRIN lenses acting as the Maxwell's Fisheye lens, Luneburg lens, and self-focusing lens are implemented. The simulated results show that the designed GP-GRIN lenses work perfectly well for focusing, collimating, and guiding the GP waves. In particular, they exhibit excellent performances in the THz regime such as broadband electrical tunability and ultra-small focusing spot of $\lambda_0/60$ (λ_0 is the wavelength of excitation light in vacuum). The proposed method allows for new opportunities in exploiting electrically tunable plasmonic elements for transformation optics at deep subwavelength scale.

Results

Structure model and analytical theory. We firstly analyze the dependence of GP waves on the surrounding environment and the Fermi energy of graphene, here considering a single layer graphene sheet surrounded by dielectrics above and below graphene with the relative permittivities of ε_{ra} and ε_{rb}, respectively. According to the Maxwell's equations and constitutive relations, the dispersion relation for the TM-polarized GP waves propagating along graphene sheet can be expressed as[23]

$$\frac{\varepsilon_{ra}}{\sqrt{\beta_p^2 - \varepsilon_{ra}\beta_0^2}} + \frac{\varepsilon_{rb}}{\sqrt{\beta_p^2 - \varepsilon_{rb}\beta_0^2}} = -\frac{i\eta_0\sigma_g}{\beta_0}, \quad (1)$$

where β_p represents the wave vector of the guided GP waves, $\beta_0 = 2\pi/\lambda_0$ is the wave vector of excitation light in vacuum, and $\eta_0 \approx 377 \ \Omega$ denotes the intrinsic impedance of vacuum. The surface conductivity of graphene σ_g is derived within the random-phase approximation and comprised of intraband and interband transitions[33,34]. In our analyses, only the intraband contribution is taken into account on condition that the half of the photon energy $\hbar\omega$ is below the Fermi energy of graphene E_f (i.e., $E_f > \hbar\omega/2$)[35]. Therefore, σ_g is simplified to a Drude form at room temperature ($T = 300$ K) with $E_f \gg k_B T$[36]

$$\sigma_g(\omega, E_f, \tau) = \frac{ie^2 E_f}{\pi\hbar^2(\omega + i\tau^{-1})}, \quad (2)$$

where ω is the angular frequency of excitation light in vacuum, e is the electron charge, k_B and $\hbar$ are the Boltzmann's constant and reduced Planck's constant, respectively. The momentum relaxation time $\tau = \mu E_f/(ev_f^2)$ is determined by the carrier mobility μ and Fermi energy E_f with the Fermi velocity $v_f = 10^6$ ms⁻¹. By substituting Eq. (2) into Eq. (1) with $\beta_p \gg \beta_0$, the propagation constant of the guided GP waves is finally obtained as

$$\beta_p(\omega, E_f, \varepsilon_{avg}) = \beta_0 \frac{2\pi\hbar^2(\omega + i\tau^{-1})\varepsilon_{avg}}{\eta_0 e^2 E_f}. \quad (3)$$

Here $\varepsilon_{avg} = (\varepsilon_{ra} + \varepsilon_{rb})/2$ is defined as the average relative permittivity of dielectrics above and below the graphene sheet. It can be seen that the mode index of the guided GP waves ($n_p = \beta_p/\beta_0$) is strongly dependent on the average relative permittivity ε_{avg} and Fermi energy E_f besides the excitation frequency ω.

The dependence of GP mode index on the permittivity of surrounded dielectric is illustrated in Fig. 1(a). It reveals that for a certain frequency larger permittivity results in higher mode index which is conducive to the achievement of a shorter wavelength of the guided GP waves. On the other hand, the dependence of GP mode index on the Fermi energy described by the gate voltage is shown in Fig. 1(b) (see Methods). It is found that the mode index of GP waves can be flexibly tuned from 5 to more than 300 by varying the gate voltage. In contrast with metal-based SPPs, the higher mode index of GP waves indicates that the deep subwavelength devices and tight confinement of energy can be easily realized on graphene. Additionally, the propagation loss of the guided GP waves can be characterized as $\text{Re}(\beta_p)/\text{Im}(\beta_p) = \omega\tau$[23]. In this context, we choose the mobility $\mu = 60000$ cm²V⁻¹s⁻¹ and Fermi energy $E_f = 0.15$ eV (corresponds to the gate voltage of 20 V), hence $\tau = 0.9$ ps, which is rather conservative to feature the practical losses of graphene[37,38]. Therefore, for the frequency of 5 THz and the Fermi energy under interband threshold, $\text{Re}(\beta_p)/\text{Im}(\beta_p) = 9\pi$, which is quite favorable compared with SPPs in metals[23].

Based on the aforementioned analyses, we propose a design of the GPQ metasurfaces for manipulating the propagation of GP waves on the 2D plane. The fundamental structure model of the metasurface incorporates a single layer graphene sheet on top of a specific PC-like dielectric layer, which consists of periodically arranged two dielectrics with unequal relative permittivities of ε_{rb1} (purple) and ε_{rb2} (grey), as presented in Fig. 2(a). A top-gate voltage is employed to adjust the carrier concentration in the graphene sheet, which allows highly tunability of the GP mode index with great ease by using Eq. (5) (see Methods). Owing to the dependence of GP mode index on the surroundings, the proposed GPQ metasurface can be equivalent

2
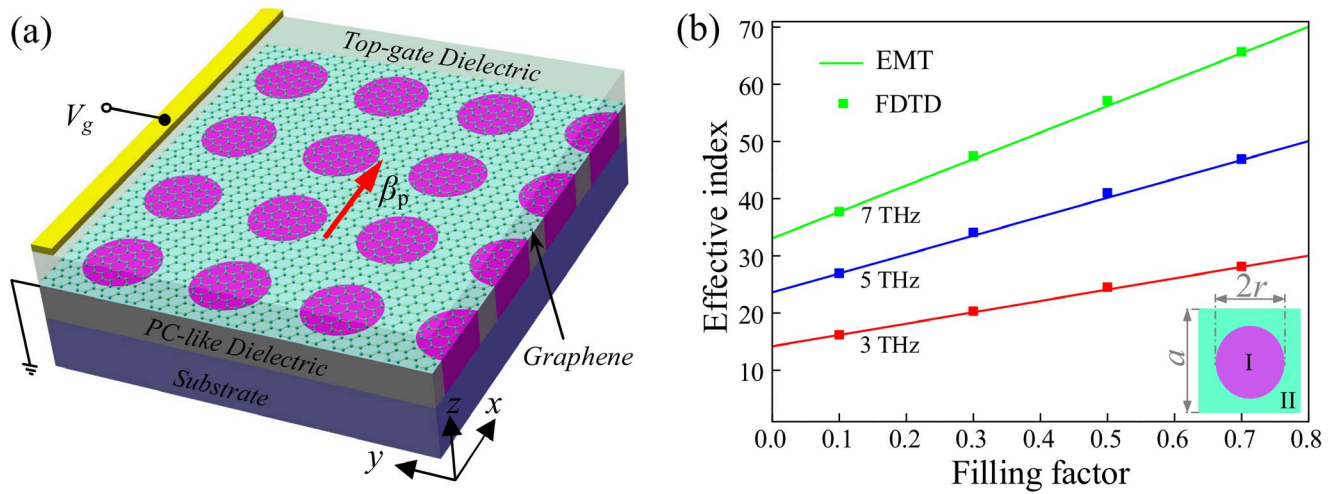
Figure 2 | Fundamental structure model and analyses of the GPQ metasurfaces. (a) Schematic of the GPQ metasurface consisting of four layers: substrate, PC-like dielectric, monolayer graphene sheet, and top-gate dielectric, wherein the gate voltage V_g is used to adjust the carrier concentration in graphene. The PC-like dielectric layer holds two dielectrics with unequal relative permittivities of ε_{rb1} (purple) and ε_{rb2} (grey). The excited GP waves propagate along the $+x$-axis direction on the graphene metasurfaces. (b) The analytical (line) and numerical (square) effective refractive indices of the GPQ metasurfaces as a function of filling factor at frequencies of 3 (red), 5 (blue), and 7 THz (green) with a gate voltage of 20 V. In the simulation, the unit cell size is always kept below one-third of the minimal GP wavelength. The inset of (b) denotes the top view of a unit cell with high (I) and low (II) mode index areas. r and a are the radius of the filling area and the period of the unit cell, respectively.

to a new material with an effective refractive index in accordance with the effective medium theory (EMT)[39,40]. The unit cell of the GPQ metasurface, as shown in the inset of Fig. 2(b), is divided into two sections: high mode index n_I area (I) and relatively low mode index n_{II} area (II), and each unit cell can be regarded as a homogeneous media within a good approximation. When the excited GP waves are guided along the graphene sheet, the effective refractive index of the unit cell is governed by[39,40]

$$n_{\text{eff}} = \gamma n_I + (1-\gamma)n_{II}. \tag{4}$$

Where $\gamma = \pi r^2/a^2$ is the filling factor, r and a are the radius of the filling area and the period of the unit cell, respectively. n_I and n_{II} are obtained by substituting $\varepsilon_{avgI} = (\varepsilon_{ra} + \varepsilon_{rb1})/2$ and $\varepsilon_{avgII} = (\varepsilon_{ra} + \varepsilon_{rb2})/2$ into Eq. (3). To demonstrate the validity of the EMT approximation, the finite-difference time-domain (FDTD) method is employed to calculate the effective refractive indices of the metasur-

faces (see Supplementary Information). According to Eq. (4), the effective refractive indices of the homogeneous GPQ metasurfaces for different incident frequencies are plotted in Fig. 2(b). It is found that the effective refractive indices from FDTD simulations are in excellent agreement with the results analytically calculated from EMT, which means that the proposed graphene-based structures can work as the metasurfaces with the effective indices described by Eq. (4). By regularly varying the filling factors of the PC-like dielectric layer, consequently, the GPQ metasurfaces with the required effective refractive index distributions can be achieved, such as the GRIN metasurfaces for transformation optics.

Numerical results. As proofs of principle, here graded GPQ metasurfaces with the GRIN distributions are implemented by employing FDTD method. Two types of classic GRIN lenses are numerically investigated on the basis of the graded GPQ metasurfaces: radial and
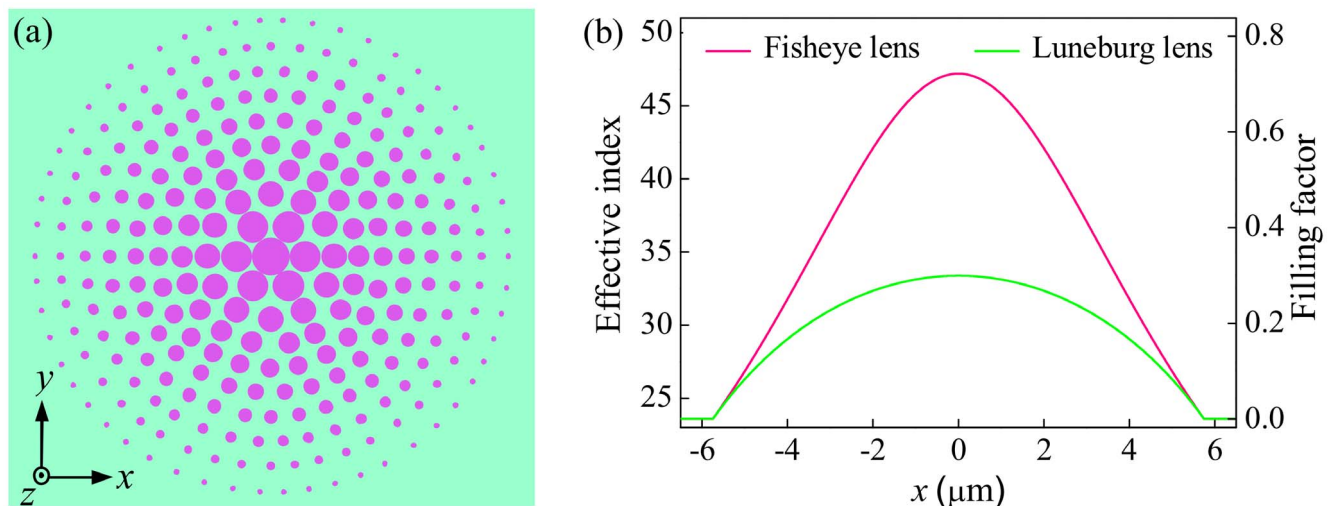
Figure 3 | Radial GP-GRIN metasurface and effective refractive index profiles. (a) Top-view illustration of the radial GP-GRIN metasurface. The filling area (purple) gradually decreases along the radial direction. (b) Lateral profiles of effective refractive index of the proposed GP Maxwell's Fisheye and Luneburg lenses as a function of filling factor. In the calculations, the frequency of the excitation light and the gate voltage are 5 THz and 20 V, respectively.
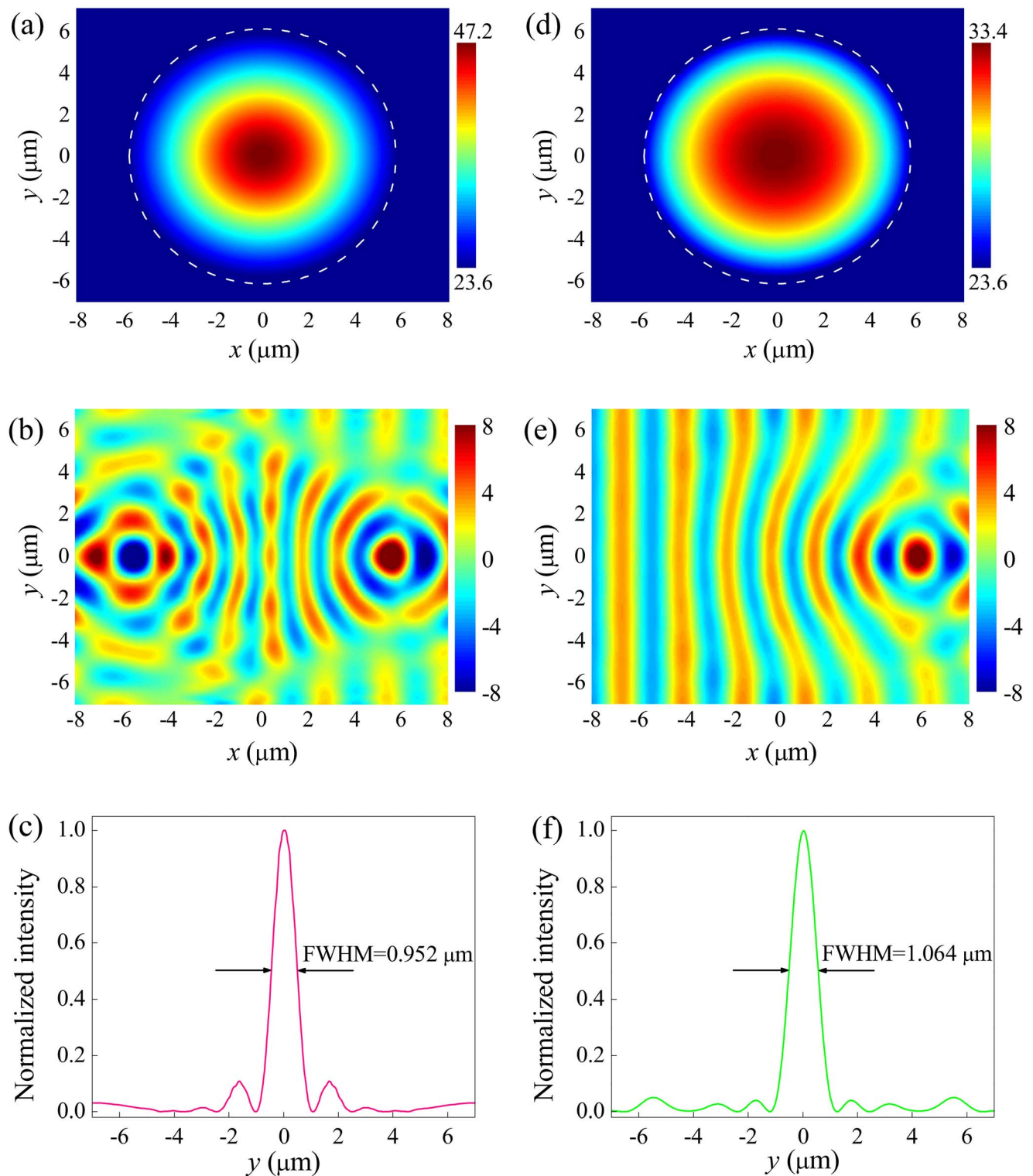
Figure 4 | 2D effective refractive index maps and numerical results. Left column: the index map (a), field distribution (b), and normalized intensity at focusing spot (c) of the GP Fisheye lens. A point source locates on the left rim of the lens. Right column: the index map (d), field distribution (e), and normalized intensity at focusing spot (f) of the GP Luneburg lens. A plane wave is launched from the left port of the lens along the +x-axis direction. The white dashed circle represents the rim of lens. The FWHMs of focusing spots at $x = 5.7$ μm along the y-axis direction for the Fisheye lens and Luneburg lens are 0.952 and 1.064 μm, respectively.

axial GP-GRIN lenses. Figure 3(a) schematically depicts the top view of the designed radial GP-GRIN metasurfaces. This design can result in the achievements of the metasurfaces with the index changing gradually along the radial direction. As the examples, 2D plasmonic Maxwell's Fisheye and Luneburg lenses based on the

radial GP-GRIN metasurfaces are demonstrated, which in general are difficult to obtain in traditional optical elements[10]. The effective refractive index profiles of the graphene-based Fisheye and Luneburg lenses, at the frequency of 5 THz, are depicted in Fig. 3(b) according to Eqs. (6) and (7) (see Methods). It can be seen that the effective GP
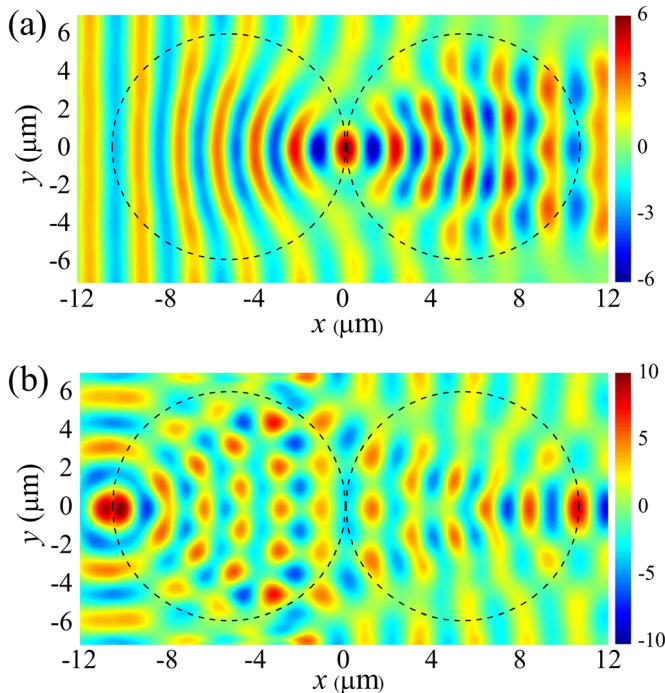
Figure 5 | Field distributions of the double-lens system based on two GP Luneburg lenses. (a) A plane wave incidents from the left port of the system. (b) A point source is set on the rim of the left lens at the position of $y = 0$. The black dashed circles denote the rim of lenses.

mode index varies gradually from 23.6 to 50 as the filling factor increases from zero to 0.8. It is worth noting that the index distributions of the Fisheye and Luneburg lenses are obtained by solely altering the filling factors with other parameters unchanged.

Being similar to the traditional Fisheye and Luneburg lenses, the plasmonic version of the Fisheye (Luneburg) lens can focus a point (plane) source to a point image on the rim of the lens[10,40–42]. Figure 4(a) illustrates the 2D effective refractive index map of the GP Fisheye lens. As it can be seen, the background index out of the lens equals 23.6 and the diameter of the lens is 11.4 μm. The mode index of GP waves at the centre of the lens approaches a maximum value of 47.2. In Fig. 4(b), the field distribution shows that when a point source is put on the rim of the Fisheye lens the corresponding image can be located at the symmetrical position of the rim. For the GP Luneburg lens, the background index as well as the lens-size is the same as that of the Fisheye lens, besides the maximum mode index of GP waves is 33.4 at the centre, as illustrated in Fig. 4(d). Figure 4(e) exhibits that a plane wave launched from the left port can be focused to a point on the opposite side of the rim. The full-width at half-maximums (FWHMs) of the focusing spots for Fisheye lens (0.952 μm) and Luneburg lens (1.064 μm), as shown in Figs. 4(c) and 4(f), are as small as $\sim\lambda_0/60$. In fact, at the rim of lens, the effective wavelength of GP waves λ_p is $\sim\lambda_0/30$. The focusing spot size is exactly a half of the effective wavelength of GP waves (i.e., $\lambda_p/2$), which is the benefit from the high mode index of GP waves. In addition, a double-lens system comprised of two Luneburg lenses with the rims touched together is simulated. The field distributions in Figs. 5(a) and 5(b) prove that the double-lens system can collimate the GP waves: only the GP waves propagating along the x-axis direction can pass through the system. Furthermore, a four-lens system is expected to realize the invisibility of the object in the centre of square, which can be regarded as a 2D cloak working similarly as the 3D cloaks[43,44] (see Supplementary Information). These results indicate that the GP Fisheye lens and Luneburg lens based on the proposed approach are potential to function as significant components

such as collimators, connectors, and cloaks in the deep subwavelength photonic circuits.

Successively, an axial GRIN lens with parabolic refractive index distribution is investigated. The axial GP-GRIN lens can be obtained by altering the filling factors along the y-axis direction. Figure 6(a) illustrates the top view of the axial GP-GRIN metasurface. According to Eqs. (4) and (8), the parabolic refractive index profile of the axial GP-GRIN lens is plotted in Fig. 6(b) (see Methods). The inset of Fig. 6(b) presents the 2D effective refractive index map of the parabolic axial GP-GRIN lens, which is similar to the refractive index distribution of the self-focusing fiber[9]. Figure 6(c) shows the self-focusing performance of the proposed lens that a plane wave propagating along the x-direction is gradually focused at the central axis ($y = 0$), and then continuous propagation results in a recovery of the plane wave. The focal length of the GP self-focusing lens is $f_1 = 7.660$ μm. Figure 6(d) shows the self-imaging performance that a point source located at $y = 2$ μm can be transferred to a point image at $y = -2$ μm, and the focal length is $f_2 = 7.465$ μm. The deviation between f_1 and f_2 can be attributed to the asymmetric scattering losses of the filling areas. The relative deviation ratio, defined as $|f_1 - f_2|/\lambda_p$, is less than 0.1. Therefore, the deviation is negligible when compared with λ_p, and the GP self-focusing lens is free of spherical aberration for focusing, imaging, and guiding the GP waves.

Although these lenses are originally designed for the frequency of 5 THz and the Fermi energy of 0.15 eV, their performances can be tuned by employing gate voltage. According to Eqs. (3) and (4), the real part of the obtained effective refractive index of the unit cell can be denoted as $n_{\text{eff}}(\omega, E_f) = \theta\omega/E_f$, wherein $\theta = 2\pi\hbar^2\{\gamma(\varepsilon_{\text{avgI}} - \varepsilon_{\text{avgII}}) + \varepsilon_{\text{avgII}}\}/(\eta_0 e^2)$ is a constant due to that once the lens is constituted the lens size and filling factor of each unit cell are kept fixed. On the basis of this relationship, $n_{\text{eff}}(\omega_1, E_f)/n_{\text{eff}}(\omega_2, E_f) = \omega_1/\omega_2$ and $n_{\text{eff}}(\omega, E_{f1})/n_{\text{eff}}(\omega, E_{f2}) = E_{f2}/E_{f1}$. Thus, the index profile is scaled by a factor of ω_1/ω_2 when the frequency is changed. Similarly, when the Fermi energy is tuned, the index profile varies by a factor of E_{f2}/E_{f1}. It indicates that the index profiles comply with Eqs. (6), (7) and (8) throughout the altering of frequency and Fermi energy, which means that the proposed lenses are dynamically tunable for wideband frequencies. Here, we take the GP Luneburg lens for example to demonstrate this excellent performance. Figure 7(a) depicts the effective refractive index profiles of the lens for different gate voltages, which agrees well with the above analyses. It is interesting that the GP waves are always focused on the rim of lens when the gate voltage is tuned, as shown in Figs. 7(b), 7(c), and 7(d), which validates that the regained metasurface is still a Luneburg lens. Additionally, it is found that when the gate voltage is varied from 15 to 5 V, the FWHMs of focusing spots for 4 THz can be reduced from 2.208 to 0.832 μm. The conclusion is drawn that the size of focusing spot can be dynamically tuned by the gate voltage while the centre of focusing spot is well maintained on the rim of lens.

Discussion
We have proposed and numerically demonstrated a flexible design of the GPQ metasurfaces for controlling the SPPs propagating along the graphene sheet by shaping dielectric layer underneath monolayer graphene into the specific PCs. It is found that the GP-GRIN metasurfaces can be constructed by employing the chirped PC-like dielectric design. To validate the feasibility and versatility of the proposed approach, the graphene metasurfaces with effective refractive index profiles of Maxwell's Fisheye lens, Luneburg lens, and self-focusing lens are numerically implemented. The simulated results demonstrate that the designed GP-GRIN lenses exhibit excellent performances in the THz regime such as focusing, collimating, and guiding the GP waves. It is found that the spot size is as small as $\sim\lambda_0/60$, and, especially, can be dynamically tuned by adjusting the gate voltage. It is interesting that the proposed lenses can work perfectly well for broadband frequencies by varying the gate voltage. We also find that
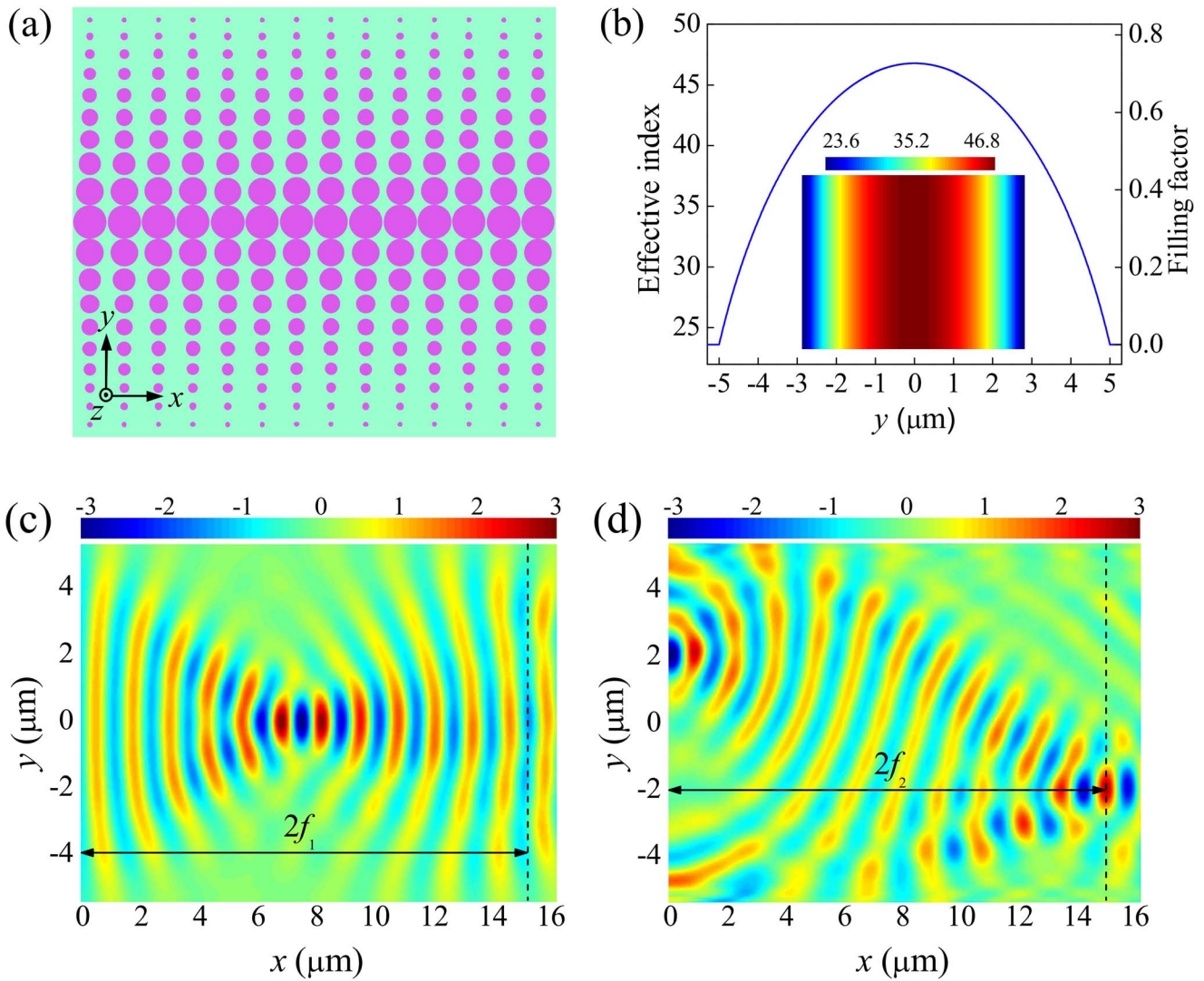
Figure 6 | Axial GP-GRIN metasurface and parabolic self-focusing lens. (a) Top-view illustration of the axial GP-GRIN metasurface. The filling area gradually decreases along the *y*-axis direction. (b) Parabolic effective refractive index profile of the proposed self-focusing lens as the function of filling factor and width. The inset of (b) shows the 2D effective refractive index map. (c) A plane wave launched from left port is recovered at right port. (d) A point source located at y = 2 μm is transferred to a point image at y = −2 μm.

the lenses can function as significant components such as collimators and connectors in the deep subwavelength photonic circuits. The proposed ultrathin planar lenses based on graphene metasurfaces are aberration-free and electrically tunable, which are really fascinating for the active integrated photonic circuits. It is predictable that the arbitrary metasurfaces with GRIN index profiles can be projected through the proposed method such as optical Janus device[45], Eaton lens[10], and magnifying lens[46], which indicates new opportunities in developing more active and complex transformational plasmonic elements.

Methods

Electrical tunability by a top-gate voltage. In the proposed GPQ metasurfaces, the carrier concentration in graphene sheet is dynamically controlled by employing a top-gate voltage, as shown in Fig. 2(a). The Fermi energy of graphene can be estimated using the parallel capacitor model as[47]

$$\left| E_f(V_g) \right| = \hbar v_f \sqrt{\pi \alpha_c \left| V_g \right|}. \tag{5}$$

Where $E_f(V_g)$ is the Fermi energy at gate voltage of V_g and $\alpha_c = \varepsilon_0 \varepsilon_{ra}/(ed)$ is the capacitor constant. In our case, the plate separation of the created capacitor d is 200 nm and the permittivity of the top-gate dielectric ε_{ra} is $3^{26,48}$. When the gate voltage is swept from 1 to 40 V, the Fermi energy experiences a sensitive variation

covering the region of interest, and hence the GP mode index changes from 5 to more than 300, as shown in Fig. 1(b). Therefore, the performance of the proposed GPQ metasurfaces can be flexibly tuned by the top-gate voltage through electric field effect.

Refractive index profiles of the proposed GP-GRIN lenses. The refractive index distributions of the traditional Maxwell's Fisheye lens and Luneburg lens are expressed as[10,41,42]

$$n(\rho) = \frac{2n_0}{1 + (\rho/R)^2}, \tag{6}$$

and

$$n(\rho) = n_0 \sqrt{2 - (\rho/R)^2}. \tag{7}$$

Where R is the radius of lens, ρ is the distance to the centre, and n_0 represents the refractive index of the background media out of the lens ($\rho > R$). The parabolic refractive index profile of the self-focusing lens is given by[9]

$$n(y) = \sqrt{n_1^2 - g^2 y^2}. \tag{8}$$

Where $g = 2(n_1^2 - n_0^2)^{1/2}/w$ is the gradient constant and w is the full-width size of the lens along the *y*-axis direction. n_0 and n_1 are the refractive indices at $|y| > w/2$ and $y = 0$, respectively. For the proposed graphene-based lenses, n_0 is the background effective refractive index of the metasurface (*i.e.*, n_{II}). The filling factor of the *j*th unit cell of the designed lens is calculated by numerically solving the equations $n_{eff}(\gamma_j) = n(\rho_j)$ and $n_{eff}(\gamma_j) = n(y_j)$ (j = 0, ±1, ±2, …).
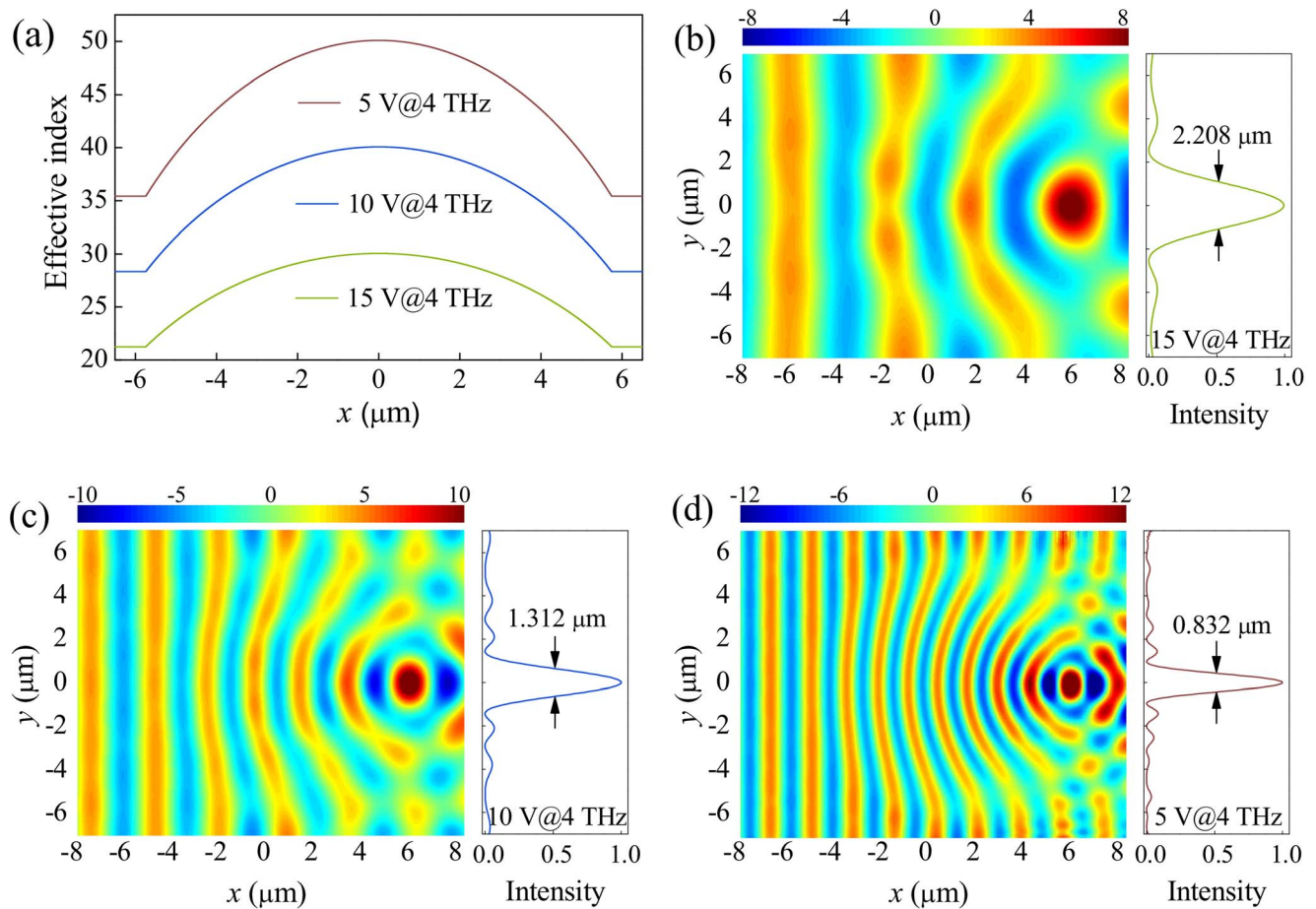
Figure 7 | Performance of the electrical tunability of the GP Luneburg lens. (a) Lateral profiles of effective refractive index of the GP Luneburg lens for the gate voltages of 5, 10, and 15 V at frequency of 4 THz. Field distributions and FWHMs of the focusing spots of the GP Luneburg lens for 15 (b), 10 (c), and 5 V (d) at frequency of 4 THz.

Numerical simulations of the designed GPQ metasurfaces. For the sake of simplicity and clarity, the single layer graphene sheet in our model is regarded as an ultra-thin metallic film with a thickness of $\Delta = 1$ nm and an equivalent relative permittivity of $\varepsilon_{gr,eq} = 1 + i\eta_0\sigma_g/(\beta_0\Delta)$[24,36]. The relative permittivities of the PC-like dielectric layer are are $\varepsilon_{rb1} = 9$ and $\varepsilon_{rb2} = 2$[26,49]. In the FDTD simulations, the minimum mesh size is set as 0.2 nm, which is small enough to ensure the numerical convergence of the results[36]. The unit cell size is kept below one-third of the minimum wavelength of the GP waves to prevent the scattering loss. The influences of PC-like dielectric on the intrinsic properties of graphene are neglected (see Supplementary Information). For the GP Maxwell's Fisheye lens and Luneburg lens, 33 unit cells are used along the radial direction and the lens size is about 11.4 μm ($R = 5.7$ μm). For the GP self-focusing lens, 27 unit cells are used along the y-axis direction and the lens width is about 10.8 μm.

1. Chen, H., Chan, C. T. & Sheng, P. Transformation optics and metamaterials. *Nat. Mater.* **9**, 387–396 (2010).
2. Schuller, J. A. *et al.* Plasmonics for extreme light concentration and manipulation. *Nat. Mater.* **9**, 193–204 (2010).
3. He, S., He, Y. & Jin, Y. Revealing the truth about 'trapped rainbow' storage of light in metamaterials. *Sci. Rep.* **2**, 583 (2012).
4. Wang, L. *et al.* Polarized linewidth-controllable double-trapping electromagnetically induced transparency spectra in a resonant plasmon nanocavity. *Sci. Rep.* **3**, 2879 (2013).
5. Liu, Y. & Zhang, X. Recent advances in transformation optics. *Nanoscale* **4**, 5277–5292 (2012).
6. Pendry, J. B., Aubry, A., Smith, D. R. & Maier, S. A. Transformation optics and subwavelength control of light. *Science* **337**, 549–552 (2012).
7. Liu, Y., Zentgraf, T., Bartal, G. & Zhang, X. Transformational plasmon optics. *Nano Lett.* **10**, 1991–1997 (2010).
8. Huidobro, P. A., Nesterov, M. L., Martín-Moreno, L. & García-Vidal, F. J. Transformation optics for plasmonics. *Nano Lett.* **10**, 1985–1990 (2010).
9. Valle, G. D. & Longhi, S. Graded index surface-plasmon-polariton devices for subwavelength light management. *Phys. Rev. B* **82**, 153411 (2010).
10. Zentgraf, T., Liu, Y., Mikkelsen, M. H., Valentine, J. & Zhang, X. Plasmonic Luneburg and Eaton lenses. *Nat. Nanotechnol.* **6**, 151–155 (2011).
11. West, P. R. *et al.* Searching for better plasmonic materials. *Laser Photon. Rev.* **4**, 795–808 (2010).
12. Zhao, C., Liu, Y., Zhao, Y., Fang, N. & Huang, T. J. A reconfigurable plasmofluidic lens. *Nat. Commun.* **4**, 2305 (2013).
13. Novoselov, K. S. *et al.* Electric field effect in atomically thin carbon films. *Science* **306**, 666–669 (2004).
14. Grigorenko, A. N., Polini, M. & Novoselov, K. S. Graphene plasmonics. *Nat. Photon.* **6**, 749–758 (2012).
15. Bonaccorso, F., Sun, Z., Hasan, T. & Ferrari, A. Graphene photonics and optoelectronics. *Nat. Photon.* **4**, 611–622 (2010).
16. Liu, M. *et al.* A graphene-based broadband optical modulator. *Nature* **474**, 64–67 (2011).
17. Liu, M., Yin, X. & Zhang, X. Double-layer graphene optical modulator. *Nano Lett.* **12**, 1482–1485 (2012).
18. Gan, X. *et al.* High-contrast electrooptic modulation of a photonic crystal nanocavity by electrical gating of graphene. *Nano Lett.* **13**, 691–696 (2013).
19. Xia, F., Mueller, T., Lin, Y. M., Valdes-Garcia, A. & Avouris, P. Ultrafast graphene photodetector. *Nat. Nanotechnol.* **4**, 839–843 (2009).
20. Fang, Z. *et al.* Graphene-antenna sandwich photodetector. *Nano Lett.* **12**, 3808–3813 (2012).
21. Gan, X. *et al.* Chip-integrated ultrafast graphene photodetector with high responsivity. *Nat. Photon.* **7**, 883–887 (2013).
22. Chen, P. Y. & Alù, A. Atomically thin surface cloak using graphene monolayers. *ACS Nano* **5**, 5855–5863 (2011).
23. Jablan, M., Buljan, H. & Soljačić, M. Plasmonics in graphene at infrared frequencies. *Phys. Rev. B* **80**, 245435 (2009).
24. Vakil, A. & Engheta, N. Transformation optics using graphene. *Science* **332**, 1291–1294 (2011).
25. Vakil, A. & Engheta, N. Fourier optics on graphene. *Phys. Rev. B* **85**, 075434 (2012).
26. Ju, L. *et al.* Graphene plasmonics for tunable terahertz metamaterials. *Nat. Nanotechnol.* **6**, 630–634 (2011).

27. Xu, H. J., Lu, W. B., Jiang, Y. & Dong, Z. G. Beam-scanning planar lens based on graphene. *Appl. Phys. Lett.* **100**, 051903 (2012).

28. Chen, J. *et al.* Optical nano-imaging of gate-tunable graphene plasmons. *Nature* **487**, 77–81 (2012).

29. Andryieuski, A., Lavrinenko, A. & Chigrin, D. Graphene hyperlens for terahertz radiation. *Phys. Rev. B* **86**, 121108(R) (2012).

30. Amin, M., Farhat, M. & Bağcı, H. A dynamically reconfigurable Fano metamaterial through graphene tuning for switching and sensing applications. *Sci. Rep.* **3**, 2105 (2013).

31. Gao, W. *et al.* Excitation and active control of propagating surface plasmon polaritons in graphene. *Nano Lett.* **13**, 3698–3702 (2013).

32. Wang, G., Liu, X., Lu, H. & Zeng, C. Graphene plasmonic lens for manipulating energy flow. *Sci. Rep.* **4**, 4073 (2014).

33. Falkovsky, L. A. & Pershoguba, S. S. Optical far-infrared properties of a graphene monolayer and multilayer. *Phys. Rev. B* **76**, 153410 (2007).

34. Hanson, G. W. Dyadic Green's functions and guided surface waves for a surface conductivity model of graphene. *J. Appl. Phys.* **103**, 064302 (2008).

35. Yao, Y. *et al.* Broad electrical tuning of graphene-loaded plasmonic antennas. *Nano Lett.* **13**, 1257–1264 (2013).

36. Wang, B., Zhang, X., García-Vidal, F. J., Yuan, X. & Teng, J. Strong coupling of surface plasmon polaritons in monolayer graphene sheet arrays. *Phys. Rev. Lett.* **109**, 073901 (2012).

37. Dean, C. R. *et al.* Boron nitride substrates for high-quality graphene electronics. *Nat. Nanotechnol.* **5**, 722–726 (2010).

38. Wang, B., Zhang, X., Yuan, X. & Teng, J. Optical coupling of surface plasmons between graphene sheets. *Appl. Phys. Lett.* **100**, 131111 (2012).

39. Choy, T. C. *Effective Medium Theory: Principles and Applications* (Oxford University Press, Oxford, 1999).

40. Dyachenko, P. N., Pavelyev, V. S. & Soifer, V. A. Graded photonic quasicrystals. *Opt. Lett.* **37**, 2178–2180 (2012).

41. Luneburg, R. *Mathematical Theory of Optics* (Brown University, Providence, 1944).

42. Cheng, Q., Ma, H. F. & Cui, T. J. Broadband planar Luneburg lens based on complementary metamaterials. *Appl. Phys. Lett.* **95**, 181901 (2009).

43. Chen, H., Wu, B. I., Zhang, B. & Kong, J. A. Electromagnetic wave interactions with a metamaterial cloak. *Phys. Rev. Lett.* **99**, 063903 (2007).

44. Chen, H. *et al.* Ray-optics cloaking devices for large objects in incoherent natural light. *Nat. Commun.* **4**, 2652 (2013).

45. Zentgraf, T., Valentine, J., Tapia, N., Li, J. & Zhang, X. An optical "Janus" device for integrated photonics. *Adv. Mater.* **22**, 2561–2564 (2010).

46. Jiang, W. X. *et al.* Broadband all-dielectric magnifying lens for far-field high-resolution imaging. *Adv. Mater.* **25**, 6963–6968 (2013).

47. Gao, W. *et al.* High-contrast terahertz wave modulation by gated graphene enhanced by extraordinary transmission through ring apertures. *Nano Lett.* **14**, 1242–1248 (2014).

48. Yamamoto, K., Tani, M. & Hangyo, M. Terahertz time-domain spectroscopy of imidazolium ionic liquids. *J. Phys. Chem. B* **111**, 4854–4859 (2007).

49. Palik, E. D. *Handbook of Optical Constants of Solids* (Academic Press, New York, 1998).

Author contributions

C.Z. conceived the idea, completed the numerical simulation, and wrote the manuscript text. X.L. discussed the design of the proposed structure model and simulation results, and supervised the whole project. G.W. improved the manuscript presentation, carried out the data analyses, and prepared part figures. All authors contributed to the scientific discussion and revision of the article.

Additional information

Supplementary information accompanies this paper at http://www.nature.com/scientificreports

Competing financial interests: The authors declare no competing financial interests.

How to cite this article: Zeng, C., Liu, X.M. & Wang, G.X. Electrically tunable graphene plasmonic quasicrystal metasurfaces for transformation optics. *Sci. Rep.* **4**, 5763; DOI:10.1038/srep05763 (2014).